

The Large Magellanic Cloud: expanding the low-mass parameter space of dark matter direct detection

Javier Reynoso-Cordova,^a Nassim Bozorgnia,^{a,b} and Marie-Cécile Piro^a

^aDepartment of Physics, University of Alberta,
CCIS 4-181, Edmonton, Alberta T6G 2E1, Canada

^bTheoretical Physics Institute, University of Alberta,
CCIS 4-181, Edmonton, Alberta T6G 2E1, Canada

E-mail: jireynos@ualberta.ca, nbozorgnia@ualberta.ca, mariecci@ualberta.ca

Abstract. We investigate how the Large Magellanic Cloud (LMC) impacts the predicted signals in near-future direct detection experiments for non-standard dark matter (DM) interactions, using the Auriga cosmological simulations. We extract the local DM distribution of a simulated Milky Way-like halo that has an LMC analogue and study the expected signals in DarkSide-20k, SBC, DARWIN/XLZD, SuperCDMS, NEWS-G, and DarkSPHERE considering DM-nucleon effective interactions, as well as inelastic DM scattering. We find that the LMC causes substantial shifts in direct detection exclusion limits towards smaller cross sections and DM masses for all non-relativistic effective field theory (NREFT) operators, with the impact being highly pronounced for velocity-dependent operators at low DM masses. For inelastic DM, where the DM particle up-scatters to a heavier state, the LMC shifts the direct detection exclusion limits towards larger DM mass splitting and smaller cross sections. Thus, we show that the LMC significantly expands the parameter space that can be probed by direct detection experiments towards smaller DM-nucleon cross sections for all NREFT operators and larger values of mass splitting for inelastic DM.

Contents

1	Introduction	1
2	Simulations	2
3	Local dark matter distribution	3
4	Dark matter direct detection	5
4.1	Halo integrals	5
4.2	Non-relativistic effective operators	6
5	Experiments	9
6	Results	10
7	Conclusions	16

1 Introduction

Cosmological and astrophysical observations from various scales have shown that a cold dark matter (DM) component is fundamental to the standard Λ CDM (Λ -cold dark matter) cosmological model [1]. Despite all the evidence, we do not yet have an unambiguous signal which sheds light onto the nature or composition of DM. Within the plateau of possible DM candidates, Weakly Interacting Massive Particles (WIMPs) are the most extensively studied due to their implications on the weak sector of the Standard Model of particle physics [2]. During the past decades, a considerable effort has been made to detect such a particle.

Direct detection experiments offer the opportunity to measure the signal that a WIMP would produce when scattering with the target nucleus or electron in an underground detector [3]. These experiments utilize different targets to explore various types of interactions probing DM masses ranging from tens of GeV up to TeV-scale [4]. However, the ongoing search for WIMPs has prompted the exploration of parameter spaces with masses lighter than the traditional 10 GeV range [5]. In particular, noble-liquid [6–12], cryogenic [13–16], and gaseous [17–20] experiments have been established as attractive detector technologies to set the most stringent constraints on the spin-independent and spin-dependent DM-nucleon cross sections for DM direct detection searches.

An important input in the analysis of direct detection results is the DM phase-space distribution in our Solar neighborhood. In the simplest and most commonly adopted halo model, the local DM velocity distribution is assumed to be a Maxwell-Boltzmann distribution with a peak speed set to the local circular speed in the Milky Way (MW). This model is known as the Standard Halo Model (SHM) [21]. The actual DM distribution, however, can be substantially different from the SHM. High resolution cosmological simulations including both DM and baryons show that although a Maxwellian velocity distribution provides a good fit to the local DM velocity distribution of simulated MW-like halos, there exists large uncertainties in the results [22–30].

One of the most significant changes to the SHM arises from the impact of the Large Magellanic Cloud (LMC) on the local DM distribution. Recent work using both cosmological [31] and idealized [32, 33] simulations have shown that the LMC can significantly boost the local DM velocity distribution to speeds greater than the escape speed from the Galaxy. This leads to substantial shifts of several orders of magnitude in the direct detection exclusion limits towards smaller cross sections and DM masses [31], especially for low mass DM. These shifts result from the existence of the DM particles originating from the LMC in the Solar neighborhood, as well as the gravitational potential of the LMC boosting the DM particles of the MW.

Given the major impact of the LMC on DM direct detection limits in the case of the simplest standard spin-independent DM-nucleon interactions, it remains to be examined how the LMC affects non-standard DM interactions. For instance several theoretical models predict the existence of mediators, which translate into a dependence of the DM-nucleon cross section on the momentum transfer or relative velocity between the DM and nucleon in the non-relativistic limit. These non-standard interactions can be described using a non-relativistic effective field theory (NREFT) approach, which parametrizes the DM-nucleus interaction in terms of a set of operators that appear in the effective Lagrangian describing the interaction [34–38]. Some of these operators lead to different dependence of the DM-nucleon cross section on the DM velocity. A modified DM velocity distribution due to the LMC can therefore have a more significant impact on direct detection limits on such DM-nucleon effective couplings. On the other hand, in the case of inelastic DM scattering [39], where DM up-scatters to a heavier state, the experiments become more sensitive to the high speed tail of the local DM velocity distribution. Consequently, the LMC’s impact on direct detection limits would be more pronounced in this case.

In this paper, we use the Auriga cosmological magneto-hydrodynamical simulations [40] to study the impact of the LMC on the interpretation of results from the next-generation direct detection experiments in the context of DM-nucleon effective interactions as well as DM inelastic scattering. In particular, we focus on six near-future experiments with different target nuclei to cover a large range of atomic mass number, A , and compare the relative changes in different experiments: DarkSide-20k [7] and SBC (Scintillating Bubble Chamber) [8] with argon ($A = 40$), DARWIN/XLZD [9, 11, 12] with xenon ($A = 131$), SuperCDMS [15] with germanium ($A = 72$), NEWS-G (New Experiments With Spheres-Gas) [17, 19] with neon ($A = 20$), and DarkSPHERE [20] with helium ($A = 4$) target nuclei. The paper is structured as follows. In section 2 we discuss the details of the simulations and the MW-LMC analogue that we use. In section 3 we present the local DM distribution of the MW analogue. In section 4 we discuss the calculations of DM direct detection signals, with the halo integrals given in section 4.1 and the NREFT operators discussed in section 4.2. In section 5 we discuss the parameters of the six near-future experiments we consider. In section 6 we present our results, and we conclude in section 7.

2 Simulations

In this work, we use the simulated MW-LMC system first studied in ref. [31]. This system is identified from the Auriga magneto-hydrodynamical simulations [40, 41]. The Auriga project [40] includes a set of zoom-in simulations of isolated MW mass halos, which were selected from a 100^3 Mpc^3 periodic cube (L100N1504) from the EAGLE project [42, 43]. The simulations were performed using the moving-mesh code Arepo [44] and implement a galaxy

formation subgrid model which includes active galactic nuclei and supernova feedback, star formation, black hole formation, metal cooling, and background UV/X-ray photoionisation radiation [40]. The simulations reproduce the observed stellar sizes, masses, rotation curves, star formation rates and metallicities of present day MW-mass galaxies. The Planck-2015 [45] cosmological parameters are adopted in the simulations: $\Omega_m = 0.307$, $\Omega_{\text{bar}} = 0.048$, $H_0 = 67.77 \text{ km s}^{-1} \text{ Mpc}^{-1}$. We use the standard resolution level (Level 4) of the simulations. At this resolution level, the DM particle mass is $m_{\text{DM}} \sim 3 \times 10^5 M_\odot$, the baryonic particle mass is $m_b = 5 \times 10^4 M_\odot$, and the Plummer equivalent gravitational softening length is $\epsilon = 370 \text{ pc}$ [46, 47].

The MW-LMC analogue used in this work is the re-simulated halo 13 in ref. [31], which corresponds to the Auriga 25 halo and its LMC analogue. This system had been re-simulated with finer snapshots close to the LMC’s pericenter approach. The MW analogue’s virial mass is $1.2 \times 10^{12} M_\odot$ and the LMC analogue’s halo mass at infall is $3.2 \times 10^{11} M_\odot$. More details about this system and its selection criteria are given in ref. [31]. We consider two snapshots for this halo: isolated MW (*Iso.*) and the present day MW-LMC (*Pres.*). *Iso.* takes place at LMC’s first apocenter before infall when the MW and LMC analogues have the largest separation, while *Pres.* is the snapshot closest to the present day separation of the observed MW and LMC system. The speed and distance of the LMC analogue with respect to the host MW analogue at the *Pres.* snapshot are 317 km/s and $\sim 50 \text{ kpc}$, respectively, which closely match the observed values.

The Sun’s position (and velocity) in the simulated halo is chosen such that it matches the observed Sun-LMC geometry, as discussed in detail in ref. [31]. In the first step, we identify the stellar disk orientations in the MW analogue that make the same angle with the orbital plane of the LMC analogues as in observations. In the second step, for each allowed disk orientation we find the Sun’s position by matching the angles between LMC’s orbital angular momentum and the Sun’s position and velocity vectors in the simulations to their observed values. In the last step, we determine the best fit Sun’s position by selecting the position that results in the closest match of the angles between the Sun’s velocity vector and the LMC’s position and velocities with their observed values.

We define the *Solar region* as the overlap of the following two regions: a spherical shell between 6 to 10 kpc from the center of the MW analogue (with the Sun at $\sim 8 \text{ kpc}$ from the galactic center) and a cone with an opening angle of $\pi/4$ radians, axis aligned with the best fit Sun’s position, and vertex at the galactic center. This region is small enough to be sensitive to the best fit Sun’s position, yet large enough to incorporate several thousand DM particles, as detailed in ref. [31]. Notice that for the *Iso.* snapshot, there is no LMC analogue and we cannot define the best fit Sun’s position. Therefore, in this case the Solar region is defined as the spherical shell with radii between 6 to 10 kpc from the center of the MW analogue.

3 Local dark matter distribution

A key ingredient for the computation of the predicted event rate in DM direct detection experiments is the astrophysical contribution (see section 4), which encompasses the local DM density and velocity distribution. The local DM density is just a normalization in the event rate, but there is a more complicated dependence of the event rate on the local DM velocity distribution, which enters through an integration. In this section, we present the

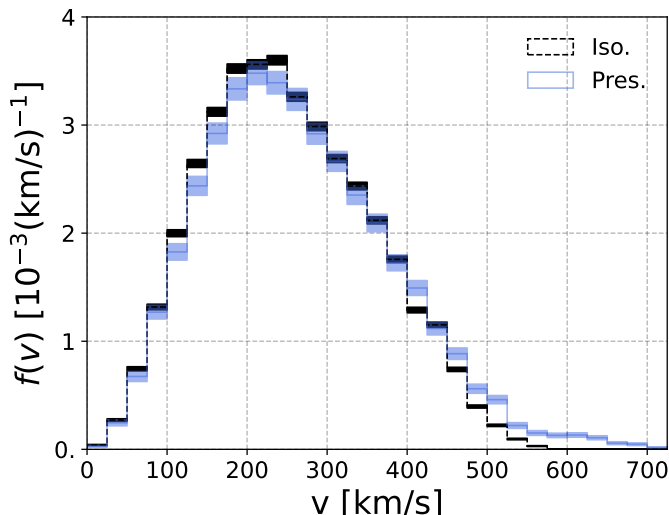


Figure 1: The local DM speed distribution in the Galactic rest frame in the Solar region for the isolated MW (black) and present day MW-LMC (blue) snapshots. The shaded bands correspond to the 1σ Poisson errors in the distributions.

DM density and velocity distribution in the Solar region (defined in section 2) extracted from the simulated MW-LMC analogue.

We define the Galactocentric reference frame with the origin on the Galactic center, the x_g -axis pointing from the Sun towards the Galactic center, the y_g -axis in the direction of the Galactic rotation, and the z_g -axis pointing towards the North Galactic Pole. The x_g - y_g plane is aligned with the Sun’s orbital plane. We specify the orientation of the (x_g, y_g, z_g) axes for the best fit Sun’s position and velocity, which results in the closest match with the observed Sun-LMC geometry (as discussed in section 2). Next, we transform the positions and velocities of the simulation particles to this Galactic reference frame.

The local DM density for the Pres. snapshot is 0.39 GeV/cm^3 , which agrees very well with the local [48–55] and global [56–63] estimates from observations. The percentage of DM particles originating from the LMC in the Solar region¹ is 0.26 for the Pres. snapshot and zero for the Iso. snapshot.

Figure 1 shows the local DM speed distribution in the Galactic rest frame for the Iso. snapshot (black) and the Pres. snapshot (blue). There are no LMC particles in the Solar region in the Iso. snapshot. The speed distributions are defined as $f(v) = v^2 \int d\Omega_{\vec{v}} \tilde{f}(\vec{v})$, where $\tilde{f}(\vec{v})$ is the normalized DM velocity distribution, $d\Omega_{\vec{v}}$ is an infinitesimal solid angle around the direction \vec{v} , and $\int dv f(v) = \int d^3v \tilde{f}(\vec{v}) = 1$. The shaded bands specify the 1σ Poisson errors in the speed distributions. Since the local circular speed of the MW is commonly set to 220 km/s in the SHM, the DM speeds in figure 1 are scaled by $(220 \text{ km/s})/v_c$, where v_c is the local circular speed of the MW analogue, calculated from the total mass contained in a sphere of radius 8 kpc. The impact of the LMC on the high speed tail of the local DM speed distribution is clearly visible at the Pres. snapshot.

¹This percentage is defined as the ratio of the number of DM particles originating from the LMC and the total number of DM particles in the Solar region, multiplied by 100.

4 Dark matter direct detection

In this section we discuss the relevant expressions and details needed to compute the predicted signals in DM direct detection experiments for non-standard DM-nucleus interactions.

4.1 Halo integrals

We consider the case of a DM particle of mass m_χ scattering with a target nucleus of mass m_T in an underground detector, and depositing the nuclear recoil energy, E_R . The differential event rate is given by

$$\frac{dR}{dE_R} = \frac{\rho_\chi}{m_\chi} \frac{1}{m_T} \int_{v>v_{\min}} d^3v \frac{d\sigma_T}{dE_R} v \tilde{f}_{\text{det}}(\vec{v}, t), \quad (4.1)$$

where ρ_χ is the local DM density, σ_T is the DM-nucleus scattering cross section, \vec{v} is the relative velocity between the DM and target nucleus, with $v = |\vec{v}|$, $\tilde{f}_{\text{det}}(\vec{v}, t)$ is the local DM velocity distribution in the detector reference frame, and v_{\min} is the minimum speed needed for the DM particle to impart a recoil energy E_R in the detector.

For the case of elastic scattering, which we consider in section 4.2, we have

$$v_{\min} = \sqrt{\frac{m_T E_R}{2\mu_{\chi T}^2}}, \quad (4.2)$$

where $\mu_{\chi T}$ is the DM-nucleus reduced mass.

For the case of inelastic DM scattering [39], the DM particle χ scatters to an excited state χ^* , with a mass difference $\delta = m_{\chi^*} - m_\chi$. We consider endothermic scattering where $\delta > 0$. We have

$$v_{\min} = \sqrt{\frac{1}{2m_T E_R} \left(\frac{m_T E_R}{\mu_{\chi T}} + \delta \right)}. \quad (4.3)$$

The dependence of v_{\min} on the mass splitting, δ , increases the minimum DM speed required for the DM particle to produce a recoil signal. We present the results for this case in section 6.

For the standard spin-independent and spin-dependent DM-nucleus interactions, the differential cross section is proportional to v^{-2} and the event rate becomes proportional to the *halo integral*,

$$\eta(v_{\min}, t) \equiv \int_{v>v_{\min}} d^3v \frac{\tilde{f}_{\text{det}}(\vec{v}, t)}{v}, \quad (4.4)$$

which along with the local DM density, ρ_χ , incorporates the astrophysical dependence of the event rate.

For the case of general non-standard interactions, such as the set of effective operators discussed in section 4.2, the differential cross section may have a different dependence on the relative velocity between the DM and the nucleus, and also vary with the exchanged momentum. In particular, for a very general set of non-relativistic effective operators, the differential cross section can be expressed as a linear combination of a velocity-dependent term and a velocity-independent term [64, 65],

$$\frac{d\sigma_T}{dE_R} = \frac{d\sigma_1}{dE_R} \frac{1}{v^2} + \frac{d\sigma_2}{dE_R}. \quad (4.5)$$

The first term results in the halo integral, $\eta(v_{\min}, t)$, given in eq. (4.4), while the second term results in a different velocity integral defined as

$$h(v_{\min}, t) \equiv \int_{v > v_{\min}} d^3v v \tilde{f}_{\text{det}}(\vec{v}, t). \quad (4.6)$$

The differential rate in eq. (4.1) can then be written as

$$\frac{dR}{dE_R} = \frac{\rho}{m_\chi} \frac{1}{m_T} \left[\frac{d\sigma_1}{dE_R} \eta(v_{\min}, t) + \frac{d\sigma_2}{dE_R} h(v_{\min}, t) \right]. \quad (4.7)$$

When the last term in eq. (4.7) is absent, we recover the standard interaction and all the astrophysical dependence of the event rate is contained solely in the halo integral, $\eta(v_{\min}, t)$. In section 4.2 we discuss the effective operators which can lead to non-standard interactions.

The LMC's influence on the local DM velocity distribution will lead to a direct impact on both $\eta(v_{\min}, t)$ and $h(v_{\min}, t)$ and thus, on the predicted signals in direct detection experiments. In order to compute these quantities, we boost the local DM velocity distribution of the simulated halo from the galactic reference frame to the detector frame, by $\tilde{f}_{\text{det}}(\vec{v}, t) = \tilde{f}_{\text{gal}}(\vec{v} + \vec{v}_s + \vec{v}_e(t))$. Here $\vec{v}_s = \vec{v}_c + \vec{v}_{\text{pec}}$ is the velocity of the Sun in the Galactic rest frame, where \vec{v}_c is the Sun's circular velocity (which we take as $v_c = |\vec{v}_c| = 220$ km/s) and $\vec{v}_{\text{pec}} = (11.10, 12.24, 7.25)$ km/s [66] is the Sun's peculiar velocity in Galactic coordinates. $\vec{v}_e(t)$ is the velocity of the Earth with respect to the Sun. We neglect the small eccentricity of the Earth's orbit, for simplicity.

We show the time averaged halo integrals $\eta(v_{\min})$ (eq. (4.4)) and $h(v_{\min})$ (eq. (4.6)) in the left and right panels of figure 2, respectively. The black and blue solid curves are the halo integrals computed from the mean value of the local DM velocity distributions shown in figure 1 for the Iso. and Pres. snapshots, respectively. In both cases the shaded bands show the 1σ uncertainty in the halo integrals and are obtained from the DM velocity distribution at 1σ from the mean. We can see that the LMC significantly impacts the high speed tails of both halo integrals in the Pres. snapshot, leading to shifts of more than 150 km/s in $\eta(v_{\min})$ and more than 160 km/s in $h(v_{\min})$.

4.2 Non-relativistic effective operators

The NREFT approach describes all possible contact DM-nucleon interactions arising from a full theory of DM [34–38]. This formalism extends the standard spin-independent and spin-dependent interactions, and includes velocity-dependent and momentum-dependent operators. In this framework, the DM-nucleus interaction is parametrized in terms of a set of independent operators, \mathcal{O}_i , listed in the first column of table 1. In this notation, \vec{q} is the momentum transferred from the DM to the nucleon, \vec{v}_\perp is the component of the relative velocity between the DM and the nucleon that is perpendicular to \vec{q} , \vec{S}_χ is the DM spin operator, \vec{S}_N is the nucleon spin operator, and m_N is the nucleon mass.

This formalism considers one-body DM-nucleon interactions mediated by a heavy spin-1 or spin-0 particle. We consider a spin-1/2 DM particle, and assume isospin independent interactions, i.e. equal couplings for protons and neutrons. We further neglect interference between different operators. The DM-nucleus differential cross section for an elastic DM interaction can then be factorized in terms of the DM response functions and the nuclear response functions [37, 67]. For isoscalar interactions, the differential cross section for the

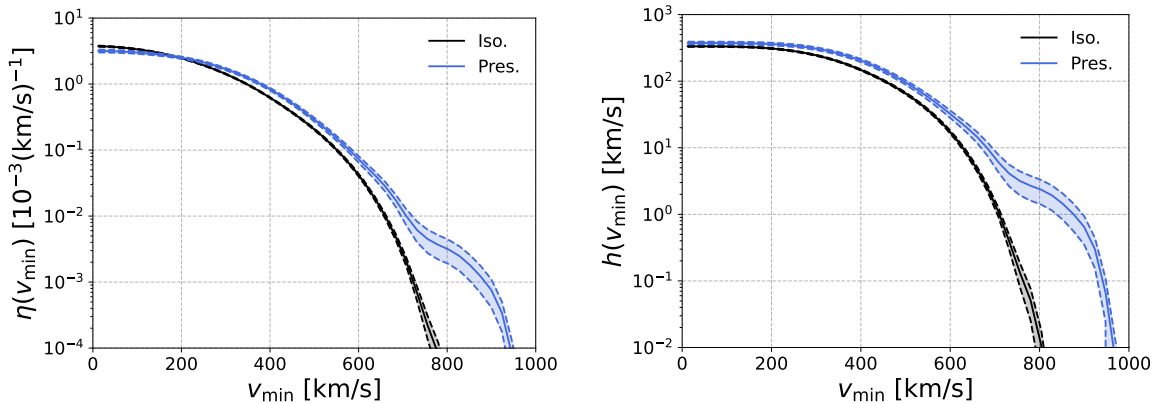


Figure 2: Time averaged halo integrals $\eta(v_{\min})$ (left panel) and $h(v_{\min})$ (right panel). The black and blue solid lines correspond to the halo integrals obtained from the mean local DM velocity distribution for the isolated MW and present day MW-LMC snapshots, respectively. The shaded bands are obtained from the local DM velocity distribution at 1σ from the mean in each case.

DM scattering with a target nucleus T is given by

$$\frac{d\sigma_T}{dE_R} = \frac{2m_T}{v^2(2J+1)} \left[\sum_{k=M,\Sigma',\Sigma''} R_k(v_{\perp}^2, q^2) W_k(q^2) + \frac{q^2}{m_N^2} \sum_{k=\Phi'',\Phi',\Delta} R_k(v_{\perp}^2, q^2) W_k(q^2) \right], \quad (4.8)$$

where J is the nuclear spin. The k index in the two sums appearing in eq. (4.8) extends over the six DM response functions, R_k , and the six nuclear response functions, W_k . Notice that since we are only considering isoscalar interactions we have dropped the superscripts $\tau = \tau' = 0$ from the usual notation of the DM and nuclear response functions and have set $R_k^{00} \equiv R_k$ and $W_k^{00} \equiv W_k$. Notice also that there are two mixed DM response functions, $R_{\Phi''M}$ and $R_{\Delta\Sigma'}$, which only appear when the couplings to at least two operators are nonzero. Since we are neglecting the combination of different operators and consider the couplings to be nonzero one at a time, these two mixed response functions are not included in eq. (4.8) and not considered in this work.

The DM response functions depend on the DM-nucleus relative velocity, the momentum transfer, and the DM-nucleon interaction strength. The nuclear response functions for a given nucleus are functions of only q^2 . These response functions are provided in the appendices of refs. [67, 68]. The differential cross section can be classified according to the powers of q^2 and v_{\perp}^2 that appear in the DM response functions. In the second column of table 1, we list the dependence of the differential cross section on powers of q^2 and v_{\perp}^2 appearing in the DM response functions, R_k , relative to the standard spin-independent \mathcal{O}_1 operator.

The experimental signatures of different NREFT operators sensitively depend on the properties of the target nucleus in the detector, as well as the DM halo. Multiple experiments have already published constraints on the WIMP-nucleon effect couplings [14, 69–73].

We would like to investigate how the LMC impacts the exclusion limits set by different near-future direct detection experiments on the couplings to the operators listed in table 1. To directly compare the results for different operators and experiments, we follow the notation

Operator	Scaling factor
$\mathcal{O}_1 = 1_\chi 1_N$	1
$\mathcal{O}_3 = i\vec{S}_N \cdot \left(\frac{\vec{q}}{m_N} \times \vec{v}_\perp \right)$	$q^2 v_\perp^2, q^4$
$\mathcal{O}_4 = \vec{S}_\chi \cdot \vec{S}_N$	1
$\mathcal{O}_5 = i\vec{S}_\chi \cdot \left(\frac{\vec{q}}{m_N} \times \vec{v}_\perp \right)$	$q^2 v_\perp^2, q^4$
$\mathcal{O}_6 = \left(\vec{S}_\chi \cdot \frac{\vec{q}}{m_N} \right) \left(\vec{S}_N \cdot \frac{\vec{q}}{m_N} \right)$	q^4
$\mathcal{O}_7 = \vec{S}_N \cdot \vec{v}_\perp$	v_\perp^2
$\mathcal{O}_8 = \vec{S}_\chi \cdot \vec{v}_\perp$	v_\perp^2, q^2
$\mathcal{O}_9 = i\vec{S}_\chi \cdot \left(\vec{S}_N \times \frac{\vec{q}}{m_N} \right)$	q^2
$\mathcal{O}_{10} = i\vec{S}_N \cdot \frac{\vec{q}}{m_N}$	q^2
$\mathcal{O}_{11} = i\vec{S}_\chi \cdot \frac{\vec{q}}{m_N}$	q^2
$\mathcal{O}_{12} = \vec{S}_\chi \cdot \left(\vec{S}_N \times \vec{v}_\perp \right)$	v_\perp^2, q^2
$\mathcal{O}_{13} = i \left(\vec{S}_\chi \cdot \vec{v}_\perp \right) \left(\vec{S}_N \cdot \frac{\vec{q}}{m_N} \right)$	$q^2 v_\perp^2, q^4$
$\mathcal{O}_{14} = i \left(\vec{S}_\chi \cdot \frac{\vec{q}}{m_N} \right) \left(\vec{S}_N \cdot \vec{v}_\perp \right)$	$q^2 v_\perp^2$
$\mathcal{O}_{15} = - \left(\vec{S}_\chi \cdot \frac{\vec{q}}{m_N} \right) \left(\left(\vec{S}_N \times \vec{v}_\perp \right) \cdot \frac{\vec{q}}{m_N} \right)$	$q^4 v_\perp^2, q^6$

Table 1: The independent operators that parametrize the DM-nucleus interaction in the NREFT approach (first column), and the scaling of the differential DM-nucleus cross section in powers of q^2 and v_\perp^2 that appear in the DM response functions, R_k , relative to the standard spin-independent \mathcal{O}_1 operator (second column).

of ref. [72], and define the effective DM-proton cross section

$$\sigma_{\chi p} \equiv \frac{(c_i^p \mu_p)^2}{\pi}, \quad (4.9)$$

where μ_p is the DM-proton reduced mass and c_i^p is the effective DM-proton coupling. For isoscalar interactions,

$$c_i^p = c_i^n = c_i^0/2, \quad (4.10)$$

where c_i^0 is the coupling to each operator \mathcal{O}_i and has dimension of $1/(\text{mass})^2$.

Notice that eq. (4.9) leads to the standard spin-independent DM-nucleon cross section for the \mathcal{O}_1 operator, but may not directly correspond to a physical cross section for the other operators.

5 Experiments

In this section, we provide the experimental parameters used to calculate the expected exclusion limits set by six near-future experiments: DarkSide-20k, SBC, DARWIN/XLZD, SuperCDMS, NEWS-G and DarkSPHERE. These experiments use different detector technologies and target nuclei as well as different nuclear energy thresholds. DarkSide-20k [7] and DARWIN/XLZD [11, 12, 74] detectors consist of double-phase time projection chambers filled with argon and xenon, respectively. The SBC experiment [8] uses a bubble chamber detector technology filled with superheated liquid argon. SuperCDMS [15] detectors use germanium and silicon cryogenic crystals cooled at millikelvin temperatures. Finally, NEWS-G [75] and DarkSPHERE are spherical proportional counters filled with noble-gas mixtures such as neon and helium, respectively.

We use the publicly available code `DDCalc` [76] to compile the results by considering the exposure, number of background and expected events, and nuclear recoil efficiencies from the following publications for consistency: Ref. [7] is used for DarkSide-20k, refs. [8, 77] for SBC, ref. [9] for DARWIN/XLZD, ref. [15] for SuperCDMS with germanium crystal, ref. [19] for NEWS-G with neon and ref. [20] for DarkSPHERE with helium. In the following, we provide the specifications considered for each experiment.

- **DarkSide-20k.** We use a total exposure of 3.65×10^7 kg · day with a total expected number of events of 0 and 1 ν -induced background event. The nuclear recoil efficiency curve is taken from figure 92 from ref. [7] within an energy range of [30 – 200] keVnr.
- **SBC.** We use a total exposure of 3.65×10^3 kg · day with a total expected number of events of 0 and 2.46 ν -induced background event [77]. The nuclear recoil efficiency curve is taken from figure 8 from ref. [78] over an energy range of [0.1 – 10] keVnr.
- **DARWIN/XLZD.** Due to the complexity of the analysis method to calculate the expected cross section limits in recent publications, such as ref. [11] often used also for DARWIN/XLZD, we decided to use the already built-in module in `DDCalc`, which follows the specifications from ref. [9]. The total exposure considered is 7.3×10^7 kg · day, and the total expected number of events is 1 with 2.37 background events. The nuclear recoil efficiency is constant with an acceptance of 30% over an energy range of [5 – 21] keVnr.
- **SuperCDMS.** We consider the high-voltage (HV) germanium detector with a total exposure of 1.6×10^4 kg · day. We take a constant efficiency of 85% acceptance and add an extra cut of 50% for the radial fiducial volume, as detailed in refs. [15, 79], within an energy range of [0.04 – 0.3] keVnr. For the background model, we use the differential rate from [15] to be a constant value of $10 \text{ keV}^{-1} \text{ kg}^{-1} \text{ yr}^{-1}$, which is a good approximation in the energy range of consideration [31, 64]. For the analysis, we assume 51 total expected events with no background event.
- **NEWS-G.** We consider only neon as the active target with a total exposure of 18 kg · day. We use a flat background of $1.65 \text{ keV}^{-1} \text{ kg}^{-1} \text{ yr}^{-1}$ [19], which gives a total expected events number of 30 with no background event. The nuclear recoil efficiency is assumed to be constant with 100% acceptance over an energy range of [0.03 – 1] keVnr.
- **DarkSPHERE.** We consider only helium (^4He isotope) as the active target with a total exposure of 7.4×10^3 kg · day. We use a flat background of $0.01 \text{ keV}^{-1} \text{ kg}^{-1} \text{ yr}^{-1}$,

Experiment	Target Nucleus	Exposure [kg· day]	Energy range [keVnr]
DarkSide-20k [7]	Ar	3.65×10^7	[30 – 200]
SBC [8]	Ar	3.65×10^3	[0.1 – 10]
DARWIN/XLZD [9]	Xe	7.3×10^7	[5 – 21]
SuperCDMS [15]	Ge	1.6×10^4	[0.04 – 0.3]
NEWS-G [19]	Ne	18	[0.03 – 1]
DarkSPHERE [20]	^4He	7.4×10^3	[0.03 – 1]

Table 2: Experimental specifications we implement in our analysis (see section 6). The columns specify i) the experiment under consideration, ii) the target nucleus we consider, iii) the total exposure in kg · day, and iv) the nuclear recoil energy range considered for each experiment in keVnr.

which gives a total expected events number of 70 with no background event [20]. As NEWS-G, the nuclear recoil efficiency is assumed to be constant with 100% acceptance within an energy range of [0.03 – 1] keVnr.

For the NEWS-G and DarkSPHERE experiments, the efficiencies are usually calculated in terms of the electron equivalent energy scale (keVee) instead of the nuclear recoil energy scale (keVnr). The conversion between these two scales is not trivial and requires several analysis steps to obtain the energy response in terms of keVnr. Using `DDCalc`, the calculation of the cross section requires the nuclear recoil efficiency. By assuming a nuclear recoil efficiency to be constant with 100% acceptance within an energy range of [0.03 – 1] keVnr, we found comparable results with the published projection limits at low WIMP masses for NEWS-G (≤ 500 MeV) [19] and DarkSPHERE (≤ 400 MeV) [20]. For higher WIMP masses, there is a constant deviation but staying within the same order of magnitude. Since the impact of the LMC mostly affects the low WIMP mass range, we consider that the nuclear recoil efficiency assumed in our analysis is a good approximation for reproducible results.

Table 2 summarizes some of the relevant quantities we outlined above for the different experiments.

6 Results

In this section we present the constraints on the effective DM-nucleon cross section (eq. (4.9)) set by the six near-future experiments described in section 5, for each of the NREFT operators given in table 1, as well as for the case of spin-independent inelastic DM scattering. In each case, we present and compare the results using the local DM velocity distribution of the isolated halo (with no LMC particles) and the present day halo (with DM particles from both the MW and LMC).

Figure 3 shows the expected exclusion limits at the 90% CL in the plane of DM mass, m_χ , and the effective DM-nucleon cross section, $\sigma_{\chi p}$, set by DarkSide-20k (top left panel), SBC (top right panel), DARWIN/XLZD (middle left panel), SuperCDMS (middle right panel), NEWS-G (bottom left panel), and DarkSPHERE (bottom right panel) for the NREFT operators. Solid lines show the limits corresponding to the local DM velocity distribution of the isolated halo (Iso.), while dashed lines show the limits for the local DM velocity distribution of the present day halo with MW and LMC DM particles (Pres.). The limits have been computed from the mean of the halo integrals (see figure 2). We have set the local DM density to $\rho_\chi = 0.3 \text{ GeV/cm}^3$ in all panels, to differentiate the impact of the local DM velocity distribution.

Notice that not all operators are present in figure 3 for the case of DarkSide-20k, SBC, NEWS-G, and DarkSPHERE since Ar, Ne, and ^4He have zero spin. This leads to zero event rates for some of the operators that depend on \vec{S}_N , and for cases in which the differential cross section depends on the nuclear response functions $W_{\Sigma'}$ and $W_{\Sigma''}$, which measure the nucleon spin content of the nucleus. However, \mathcal{O}_3 , \mathcal{O}_{12} and \mathcal{O}_{15} , which contain \vec{S}_N , can still produce a nuclear recoil in Ar and Ne, since for these operators the nuclear response function $W_{\phi''}$ is sensitive to the nucleon spin-orbit coupling. For ^4He , the $W_{\phi''}$ nuclear response function does not appear, and the only operators present are therefore \mathcal{O}_1 , \mathcal{O}_5 , \mathcal{O}_8 and \mathcal{O}_{11} .

As seen in figure 3, the exclusion limits are shifted towards smaller DM masses and smaller cross sections due to the impact of the LMC. This trend exists for all the operators and experiments we consider, and is more pronounced at small DM masses. This is expected, since the variations in the tails of the halo integrals at high v_{\min} (shown in figure 2) lead to the differences in the exclusion limits at low DM masses. This also agrees with the results of refs. [31, 32] for the standard spin-independent interaction. The LMC, therefore, increases the sensitivity of direct detection experiments at low DM masses.

To further quantify the impact of the LMC on the exclusion limits, in the left panels of figures 4-9, we present the ratio of the upper limit at the 90% CL on the effective DM-nucleon cross section for the isolated halo, $\sigma_{\chi p}^{\text{iso}}$, and for the present day halo, $\sigma_{\chi p}^{\text{pres}}$, for different operators for DarkSide-20k, SBC, DARWIN/XLZD, SuperCDMS, NEWS-G, and DarkSPHERE, respectively. Each ratio curve starts at the lowest DM mass where the ratio is finite. Below that mass, the recoil energy produced from the DM scattering in the detector is below the energy threshold of the experiment. From these plots, we can therefore quantify how the LMC impacts the exclusion limits for each operator and for the range of DM masses probed by the experiments. The right panels of figures 4-9 show the same ratio, $\sigma_{\chi p}^{\text{iso}}/\sigma_{\chi p}^{\text{pres}}$, evaluated at two fixed DM masses. The blue circles show the ratios evaluated at the minimum DM mass, m_χ^* , for which $\sigma_{\chi p}^{\text{iso}}$ is finite for *all* operator. The value of m_χ^* for each experiment is specified with a dashed gray line in the left panels of the figures and given as a legend on the top right corner of the right panels. The orange circles show the ratios evaluated at a slightly larger but arbitrary DM mass, specified on the bottom right corner of the plots in the right panels. The ratio $[\sigma_{\chi p}^{\text{iso}}/\sigma_{\chi p}^{\text{pres}}]_{m_\chi}$, therefore, allows us to compare the impact of the LMC on the exclusion limits for different operators, at two fixed small DM masses close to the minimum mass that can be probed by each experiment for each operator.

The dashed colored lines in the left panels and the open circles in the right panels of figures 4-9 identify operators for which the DM-nucleon cross section has a velocity dependent scaling compared to \mathcal{O}_1 , as listed in the second column of table 1. Notice that for Ar, Ne, and ^4He which do not have spin, only operators \mathcal{O}_5 and \mathcal{O}_8 lead to a velocity-dependent scaling of the cross section. For \mathcal{O}_3 , \mathcal{O}_{12} , and \mathcal{O}_{15} in case of Ar and Ne, only the q -dependent terms

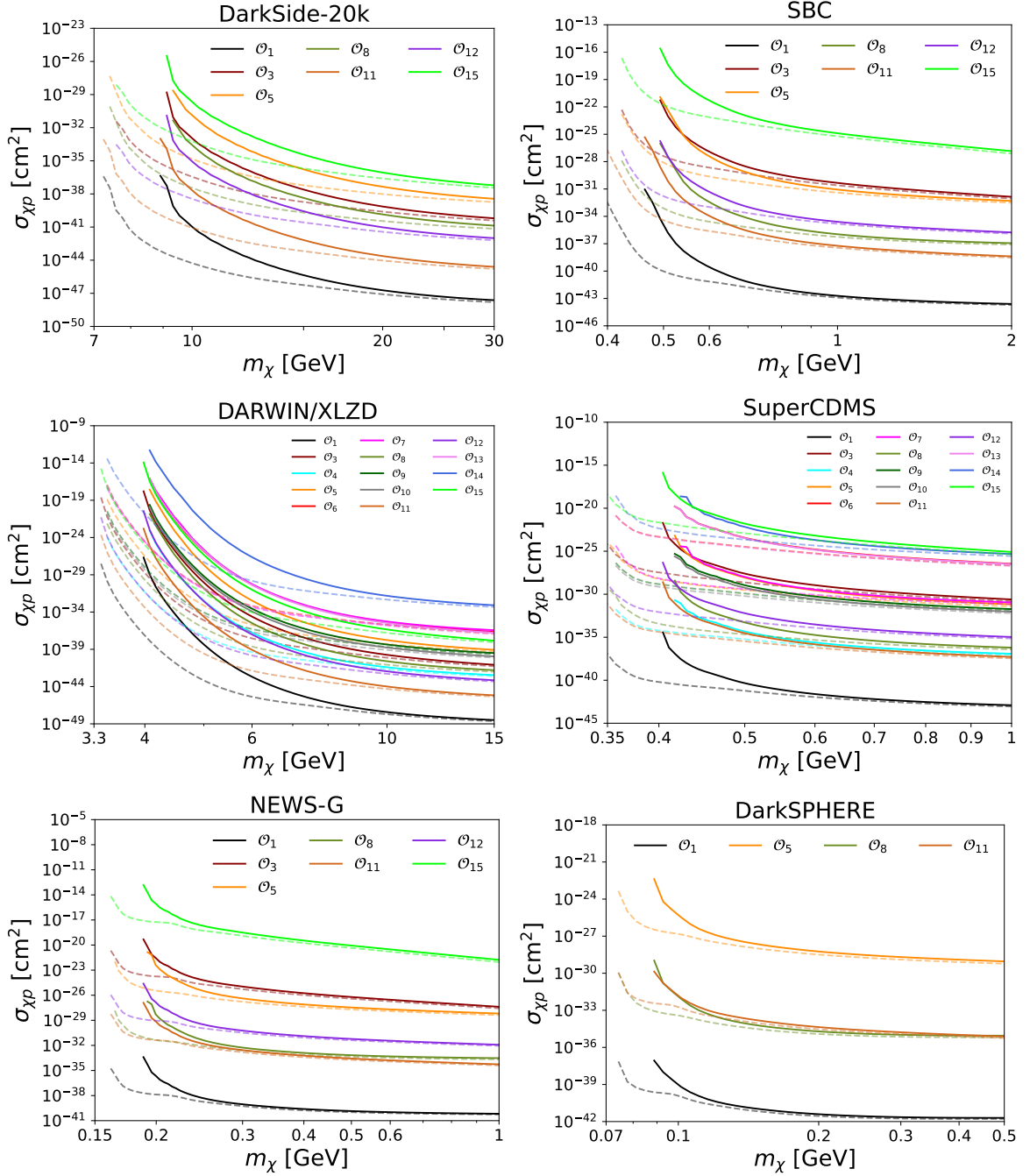


Figure 3: Exclusion limits at the 90% CL in the DM mass and the effective DM-nucleon cross section plane for DarkSide-20k (top left panel), SBC (top right panel), DARWIN/XLZD (middle left panel), SuperCDMS (middle right panel), NEWS-G (bottom left panel), and DarkSPHERE (bottom right panel) for the different NREFT operators, \mathcal{O}_i , discussed in section 4.2. Solid colored lines are computed using the local DM velocity distribution of the isolated MW analogue, while dashed colored lines are computed for the present day MW-LMC analogue. The local DM density is set to $\rho_\chi = 0.3$ GeV/cm³.

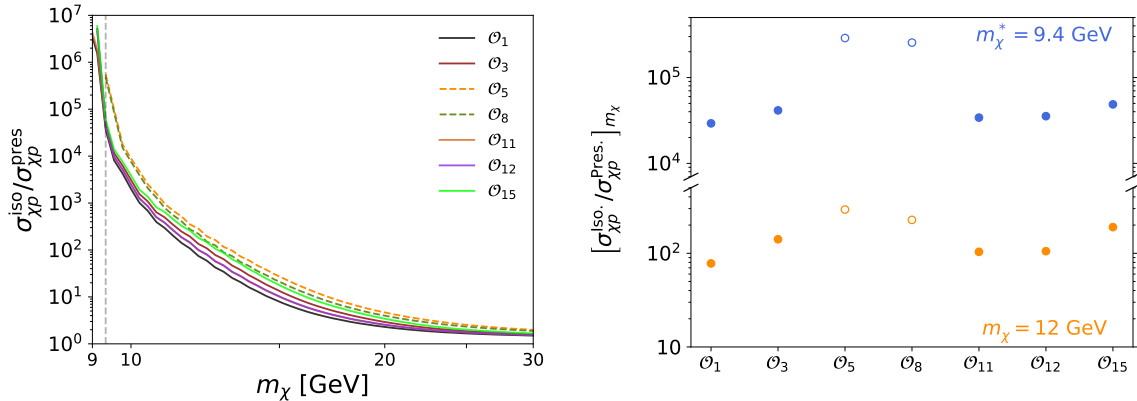


Figure 4: Left panel: The ratio of the exclusion limit at the 90% CL on the effective DM-nucleon cross section obtained using the local DM distribution of the isolated MW, $\sigma_{\chi p}^{\text{iso}}$, and that of the present day MW-LMC, $\sigma_{\chi p}^{\text{pres}}$, for DarkSide-20k and for different NREFT operators. Each ratio curve starts at the lowest DM mass where the ratio is finite. Right panel: The ratio $\sigma_{\chi p}^{\text{iso}}/\sigma_{\chi p}^{\text{pres}}$ evaluated at two fixed DM masses. The blue circles show the ratios evaluated at the minimum DM mass, m_χ^* , for which $\sigma_{\chi p}^{\text{iso}}$ is finite for all operators. The value of m_χ^* is specified with a gray dashed vertical line in the left panel and given as a legend in the top corner of the right panel. The orange circles show the ratios evaluated at a slightly larger DM mass, whose value is specified in the bottom corner of the right panel. The dashed (solid) colored lines in the left panel and the open (filled) circles in the right panel correspond to operators for which the DM-nucleus cross section has a velocity-dependent (velocity-independent) scaling compared to the \mathcal{O}_1 operator.

are present in this scaling.

At a fixed DM mass close to the minimum mass probed by each experiment, the impact of the LMC tends to be larger for operators that lead to a velocity-dependent scaling in the DM-nucleus cross section. This is clearly the case for \mathcal{O}_5 and \mathcal{O}_8 for all six experiments. As shown in figures 4-9, $[\sigma_{\chi p}^{\text{iso}}/\sigma_{\chi p}^{\text{pres}}]_{m_\chi^*}$ reaches $\sim 3 \times 10^5$ at $m_\chi^* = 9.4$ GeV for DarkSide-20k, $\sim 10^7$ at $m_\chi^* = 0.49$ GeV for SBC, $\sim 4 \times 10^9$ at $m_\chi^* = 4.1$ GeV for DARWIN/XLZD, $\sim 10^3$ at $m_\chi^* = 0.44$ GeV for SuperCDMS, $\sim 3 \times 10^4$ at $m_\chi^* = 0.19$ GeV for NEWS-G, and 10^4 at $m_\chi^* = 0.088$ GeV for DarkSPHERE. For DARWIN/XLZD and SuperCDMS which are sensitive to all operators, the LMC's impact is also large for operators \mathcal{O}_7 and \mathcal{O}_{14} (in addition to \mathcal{O}_5 and \mathcal{O}_8) across a range of DM masses up to ~ 15 GeV in DARWIN/XLZD and ~ 1 GeV in SuperCDMS. Notice that the value of the ratio $\sigma_{\chi p}^{\text{iso}}/\sigma_{\chi p}^{\text{pres}}$ is sensitive to the DM mass at which it is evaluated. The ordering of this ratio for different operators, shown in the right panels of figures 4-9, is especially impacted by the exact value of m_χ .

Besides the case of non-standard DM interactions using NREFT, we have also studied the impact of the LMC on the standard spin-independent DM-nucleon cross section for the case of inelastic DM. In this case, the minimum DM speed, v_{min} (given in eq. (4.3)) depends on the mass splitting, δ , between the lighter and heavier DM states. To quantify the effect of the LMC on the cross section for a range of values of δ , we first fix the DM mass, taking two representative values for each experiment. Figure 10 shows the exclusion limits at the 90% CL in the plane of δ and the standard spin-independent DM-nucleon cross section, $\sigma_{\chi p}$, for DarkSide-20k (green lines), SBC (magenta lines), DARWIN/XLZD (orange lines),

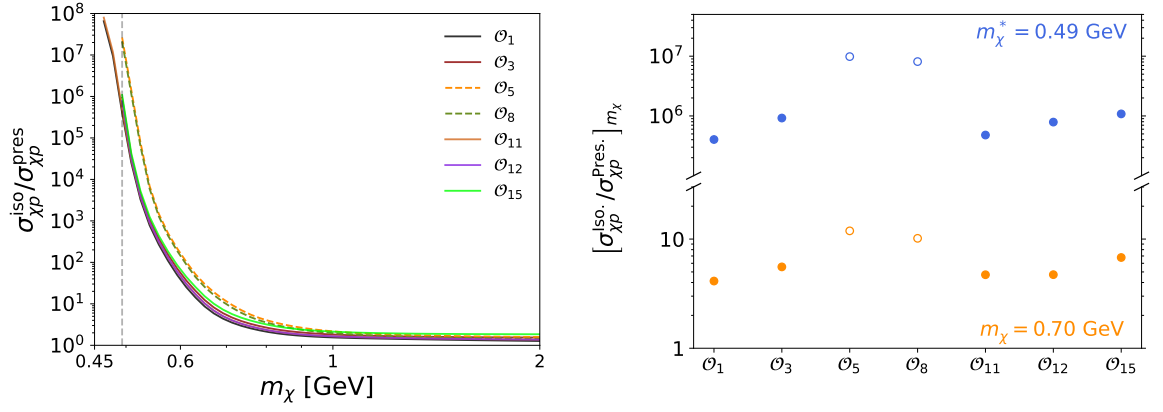


Figure 5: Same as figure 4, but for the SBC experiment.

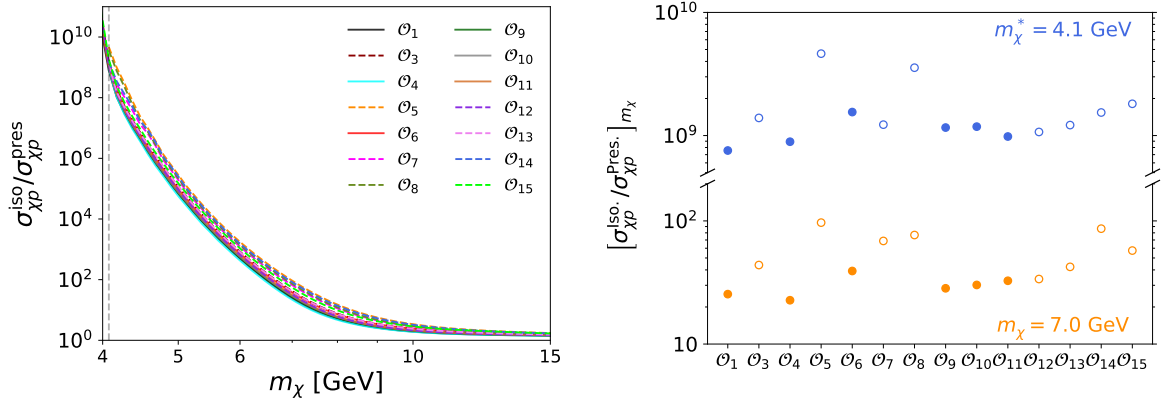


Figure 6: Same as figure 4, but for the DARWIN/XLZD experiment.

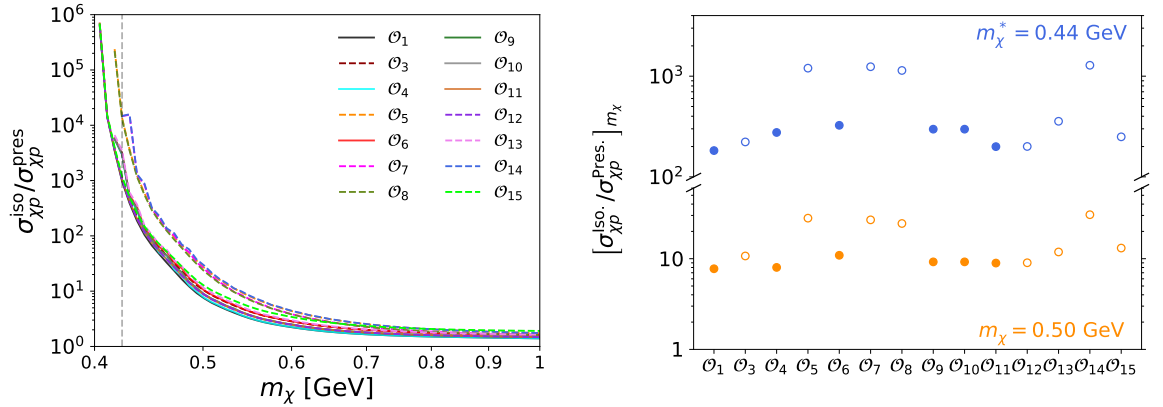


Figure 7: Same as figure 4, but for the SuperCDMS experiment.

SuperCDMS (black lines), NEWS-G (blue lines), and DarkSPHERE (red lines). For each experiment, the darker colored lines show the results for a smaller DM mass (1, 10, or 100

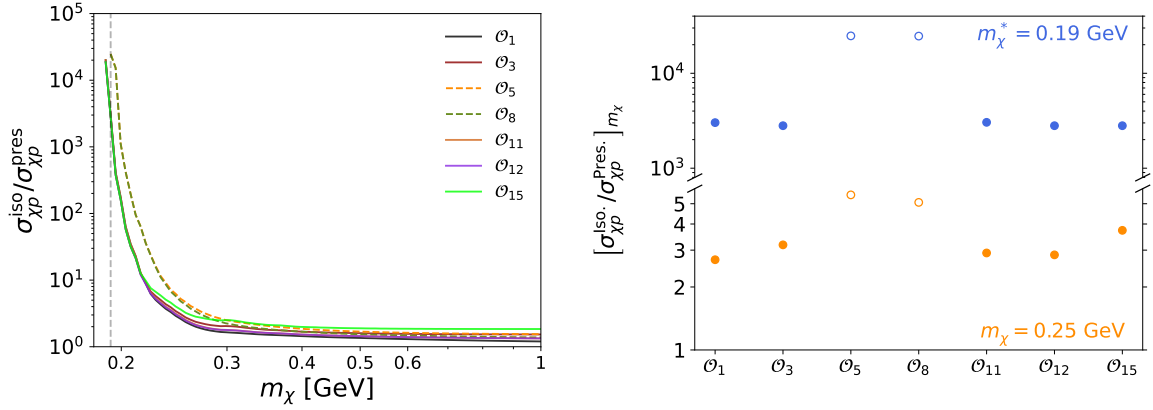


Figure 8: Same as figure 4, but for the NEWS-G experiment.

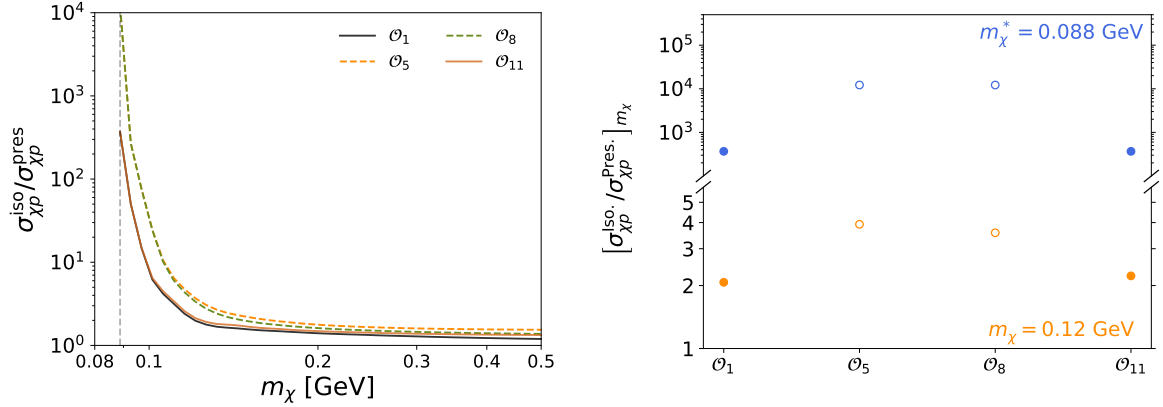


Figure 9: Same as figure 4, but for the DarkSPHERE experiment.

GeV depending on the experiment), and the lighter colored lines show the results for a larger DM mass (10, 100, or 1000 GeV depending on the experiment). The solid lines show the limits for the isolated MW analogue, while the dashed lines show the limits for the present day MW-LMC analogue.

For all six experiments and choices of DM mass considered in figure 10, the LMC shifts the exclusion limits towards larger mass splittings, δ , and smaller cross sections, $\sigma_{\chi p}$. The LMC, therefore, increases the sensitivity of the experiments for probing larger values of δ in the case of inelastic DM. For each experiment, the impact of the LMC is more significant at larger δ values, where the experiment probes higher v_{min} and the sensitivity to the high speed tail of the halo integrals increases. Additionally, the LMC has a larger impact for experiments that have a more massive target nucleus, since they can probe a larger range of DM velocities and are sensitive to larger δ values. We can see from figure 10 that at a fixed large cross section, e.g. $\sigma_{\chi p} = 10^{-34} \text{ cm}^2$, and for both $m_\chi = 100$ and 1000 GeV, the LMC shifts the exclusion limits by ~ 40 keV towards larger δ values for DARWIN/XLZD, which has the most massive target nucleus (i.e. Xe) among the six experiments considered. For SuperCDMS and DarkSide, the exclusion limits shift by at most ~ 35 keV for the masses considered. For SBC, NEWS-G, and DarkSPHERE, the shifts are at most ~ 15 keV, ~ 5 keV, and ~ 0.15 keV,

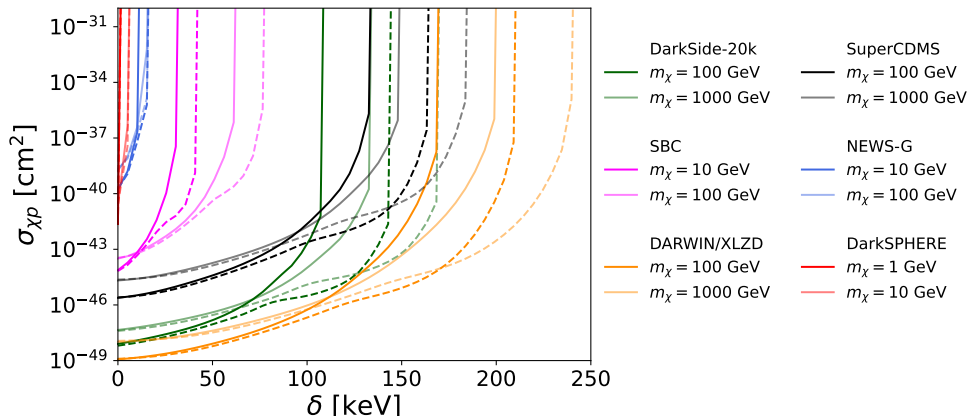


Figure 10: Exclusion limits at the 90% CL in the plane of the mass splitting, δ , for inelastic DM and the standard spin-independent DM-nucleon cross section, $\sigma_{\chi p}$, for DarkSide-20k (green lines), SBC (magenta lines), DARWIN/XLZD (orange lines), SuperCDMS (black lines), NEWS-G (blue lines), and DarkSPHERE (red lines). The darker (lighter) colored lines show the limits for a 100 GeV (1000 GeV) DM mass for DarkSide-20k, DARWIN/XLZD and SuperCDMS, a 10 GeV (100 GeV) DM mass for SBC and NEWS-G, and a 1 GeV (10 GeV) DM mass for DarkSPHERE. Solid colored lines are computed using the local DM velocity distribution of the isolated MW, while dashed colored lines are computed for the present day MW-LMC analogue. The local DM density is set to $\rho_\chi = 0.3 \text{ GeV}/\text{cm}^3$.

respectively, for the masses considered.

Figure 11 shows the exclusion limits at the 90% CL in the m_χ and $\sigma_{\chi p}$ plane for different values of the mass splitting δ for DarkSide-20k (top left panel), SBC (top right panel), DARWIN/XLZD (middle left panel), SuperCDMS (middle right panel), NEWS-G (bottom left panel), and DarkSPHERE (bottom right panel). The solid lines show the limits for the isolated MW, while the dashed lines show the limits for the present day MW-LMC. Similar to our results for the case of the NREFT operators, the LMC causes a shift in the exclusion limits towards smaller DM masses and smaller cross sections for inelastic DM. The effect is more prominent for larger values of δ , as expected.

We can see again from figure 11 that the LMC extends the parameter space that can be probed by the experiments for inelastic DM. For instance, for the isolated MW, the mass splitting of $\delta = 150 \text{ keV}$ is not accessible to DarkSide-20k. However, when the impact of the LMC is included (i.e. for the present day MW-LMC analogue), DarkSide-20k can probe this mass splitting. Similarly, mass splittings of $\delta = 70, 225, 175, 18,$ and 7 keV , become accessible to the SBC, DARWIN/XLZD, SuperCDMS, NEWS-G, and DarkSPHERE experiments, respectively, only when the impact of the LMC is considered.

7 Conclusions

In this work we have studied the impact of the LMC on the interpretation of results from near-future direct detection experiments for non-standard DM interactions, using a simulated MW-LMC system from the Auriga magneto-hydrodynamical simulations. In particular, we investigated how the LMC affects the predicted signals in DarkSide-20k, SBC, DARWIN/XLZD, SuperCDMS, NEWS-G, and DarkSPHERE, considering DM-nucleon effective inter-

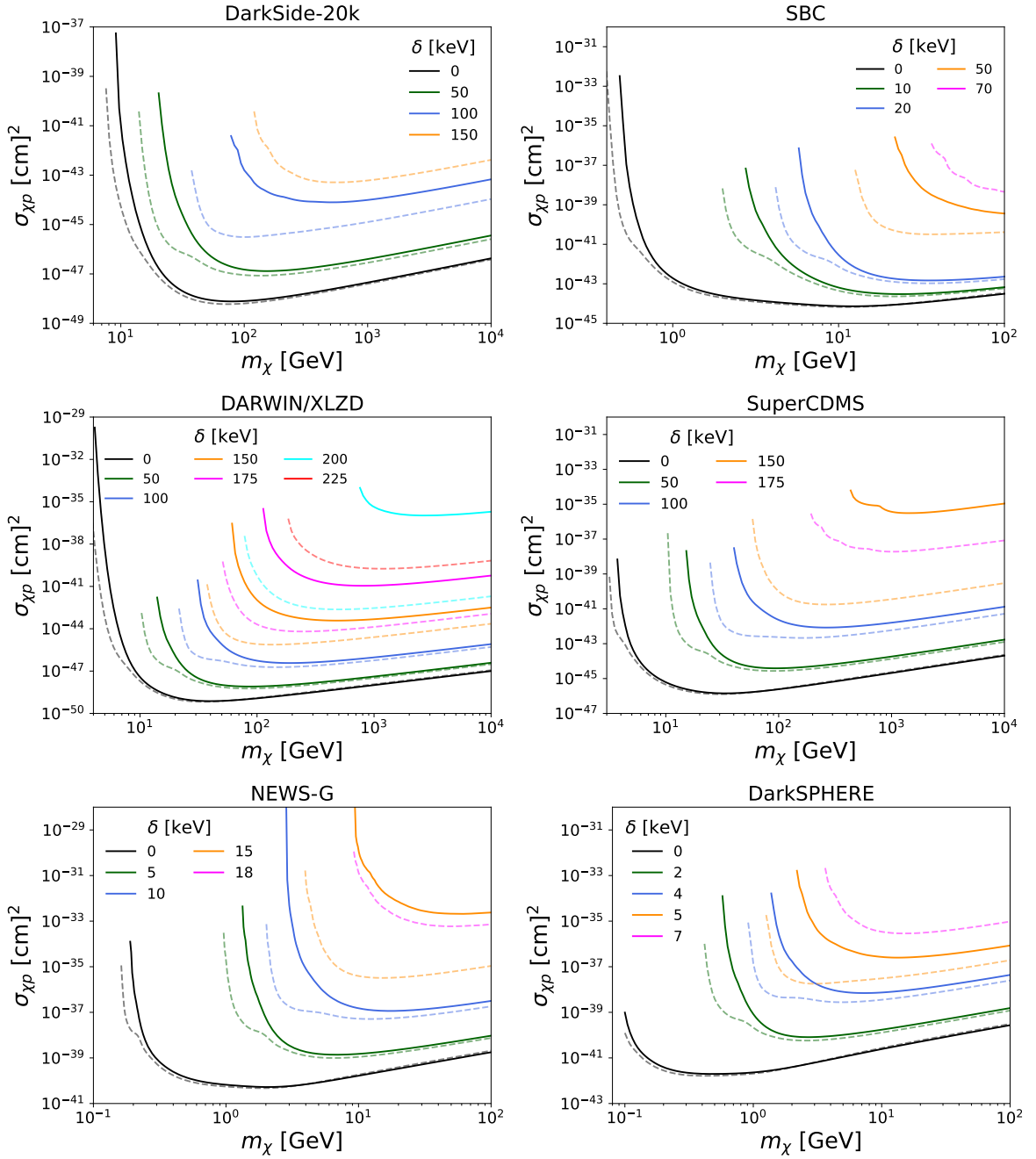


Figure 11: Exclusion limits at the 90% CL in the plane of the DM mass, m_χ , and the standard spin-independent DM-nucleon cross section, $\sigma_{\chi p}$, for DarkSide-20k (top left panel), SBC (top right panel), DARWIN/XLZD (middle left panel), SuperCDMS (middle right panel), NEWS-G (bottom left panel), and DarkSPHERE (bottom right panel). Different colored lines correspond to different values of the DM mass splitting, δ , as specified in the legends. Solid colored lines are computed using the local DM velocity distribution of the isolated MW, while dashed colored lines are computed for the present day MW-LMC analogue. The local DM density is set to $\rho_\chi = 0.3 \text{ GeV/cm}^3$.

actions using the NREFT approach, as well as inelastic DM scattering. These experiments use different detector technologies and target nuclei, and as a result have different sensitivities to various NREFT operators, as well as the impact of the LMC.

We utilized the simulated MW-LMC system first studied in ref. [31] and compared our results for two simulation snapshots: the isolated MW analogue (before the infall of the LMC into the MW), and the present day MW-LMC analogue. As shown in previous work employing both cosmological and idealized simulations [31–33], the LMC significantly boosts the high speed tail of the local DM velocity distribution. This leads to a shift of ~ 150 km/s in the tails of the halo integrals, η (eq. (4.4)) and h (eq. (4.6)), towards higher speeds. These two halo integrals encode the dependence of the direct detection event rate on the local DM velocity distribution for general non-standard DM interactions.

The shifts in the high speed tails of the halo integrals due to the influence of the LMC cause significant shifts in direct detection exclusion limits towards smaller effective DM-nucleon cross sections and DM masses for all NREFT operators and the six experiments considered. As expected, the impact of the LMC tends to be more pronounced for operators that lead to a velocity-dependent scaling in the DM-nucleus cross section. For the case of the DarkSide-20k, SBC, NEWS-G, and DarkSPHERE experiments which employ spin zero Ar, Ne, and ^4He targets, the greatest shifts in the exclusion limits occur for the two velocity-dependent operators present, \mathcal{O}_5 and \mathcal{O}_8 . In particular, the exclusion limits shift by more than 5 orders of magnitude in DarkSide-20k at a DM mass of ~ 9 GeV, 7 orders of magnitude in SBC at ~ 0.5 GeV, more than 4 orders of magnitude in NEWS-G at ~ 0.2 GeV, and 4 orders of magnitude in DarkSPHERE at ~ 0.09 GeV.

For the case of DARWIN/XLZD and SuperCDMS, the largest impact on the exclusion limits happens for the velocity-dependent \mathcal{O}_5 , \mathcal{O}_7 , \mathcal{O}_8 , and \mathcal{O}_{14} operators across a range of DM masses up to ~ 15 GeV for DARWIN/XLZD and up to ~ 1 GeV for SuperCDMS. At the lowest DM mass that can be probed by all operators, the largest shifts in the exclusion limits occur for \mathcal{O}_5 and \mathcal{O}_8 in DARWIN/XLZD, where the limits shift by more than 9 orders of magnitude at a DM mass of ~ 4 GeV. For SuperCDMS, operators \mathcal{O}_5 , \mathcal{O}_7 , \mathcal{O}_8 , and \mathcal{O}_{14} , show a similar shift of 3 orders of magnitude at ~ 0.4 GeV. In both experiments, the remaining velocity-dependent operators, \mathcal{O}_3 , \mathcal{O}_{12} , \mathcal{O}_{13} , and \mathcal{O}_{15} , show a smaller but still significant shift in the cross sections. The shift for this latter group of velocity-dependent operators becomes comparable to that for a number of velocity-independent operators, such as \mathcal{O}_6 , which has a q^4 scaling in the cross section.

We also studied the impact of the LMC on direct detection of inelastic DM scattering, where the DM particle up-scatters to a heavier state with a mass splitting δ . At a fixed DM mass, the LMC significantly shifts the direct detection exclusion limits towards smaller cross sections and larger δ , with the impact being more pronounced for experiments with a more massive target nucleus. Considering a fixed δ value, the exclusion limits are shifted towards smaller DM masses and smaller cross sections by several orders of magnitude, due to the impact of the LMC. The LMC, therefore, allows the experiments to probe higher values of δ . In particular, because of LMC’s impact, DARWIN/XLZD, SuperCDMS, DarkSide, SBC, NEWS-G, and DarkSPHERE would be able to probe δ values as large as 225, 175, 150, 70, 18, and 7 keV, respectively.

Our results demonstrate that the presence of the LMC significantly expands the low-mass parameter space that can be probed by direct detection experiments towards smaller DM-nucleon cross sections, for all NREFT operators. Furthermore, the LMC greatly enhances the experiments’ sensitivity to larger values of the mass splitting for inelastic DM.

Acknowledgments

JR and NB acknowledge the support of the Natural Sciences and Engineering Research Council of Canada (NSERC), funding reference number RGPIN-2020-07138, and the NSERC Discovery Launch Supplement, DGEGR-2020-00231. NB acknowledges the support of the Canada Research Chairs Program. We thank Azadeh Fattahi for providing the re-simulated Auriga halo studied in this work. We thank Daniel Durnford for fruitful discussions regarding the cross-sections for NEWS-G and DarkSPHERE experiments. We also thank Knut Dundas Morå for helpful discussion regrading DARWIN/XLZD cross-section limits. We thank, as well, Simon Viel, Shawn Westerdale and Ariel Zuñiga Reyes for helpful discussion on the NREFT operators obtained for the DEAP experiment.

References

- [1] **Planck** Collaboration, N. Aghanim et al., *Planck 2018 results. VI. Cosmological parameters*, *Astron. Astrophys.* **641** (2020) A6, [[arXiv:1807.06209](#)]. [Erratum: *Astron. Astrophys.* 652, C4 (2021)].
- [2] J. L. Feng, *Dark matter candidates from particle physics and methods of detection*, *Annu. Rev. Astron. Astrophys.* **48** (2010) 495–545.
- [3] M. W. Goodman and E. Witten, *Detectability of Certain Dark Matter Candidates*, *Phys. Rev. D* **31** (1985) 3059.
- [4] G. Jungman, M. Kamionkowski, and K. Griest, *Supersymmetric dark matter*, *Phys. Rept.* **267** (1996) 195–373, [[hep-ph/9506380](#)].
- [5] A. K. Drukier and S. Nussinov, *Towards Detection of Low Mass WIMPs ($M_{\text{WIMP}} < 10 \text{ GeV}/c^2$): Mini-Review*, *Int. J. Mod. Phys. A* **28** (2013) 1330033.
- [6] **DarkSide-50** Collaboration, P. Agnes et al., *Search for low-mass dark matter WIMPs with 12 ton-day exposure of DarkSide-50*, *Phys. Rev. D* **107** (2023), no. 6 063001, [[arXiv:2207.11966](#)].
- [7] **DarkSide-20k** Collaboration, C. E. Aalseth et al., *DarkSide-20k: A 20 tonne two-phase LAr TPC for direct dark matter detection at LNGS*, *Eur. Phys. J. Plus* **133** (2018) 131, [[arXiv:1707.08145](#)].
- [8] E. Alfonso-Pita et al., *Scintillating Bubble Chambers for Rare Event Searches*, *Universe* **9** (2023), no. 8 346.
- [9] M. Schumann, L. Baudis, L. Bütikofer, A. Kish, and M. Selvi, *Dark matter sensitivity of multi-ton liquid xenon detectors*, *JCAP* **10** (2015) 016, [[arXiv:1506.08309](#)].
- [10] **XENON** Collaboration, E. Aprile et al., *First Dark Matter Search with Nuclear Recoils from the XENONnT Experiment*, *Phys. Rev. Lett.* **131** (2023), no. 4 041003, [[arXiv:2303.14729](#)].
- [11] J. Aalbers et al., *A next-generation liquid xenon observatory for dark matter and neutrino physics*, *J. Phys. G* **50** (2023), no. 1 013001, [[arXiv:2203.02309](#)].
- [12] L. Baudis, *DARWIN/XLZD: A future xenon observatory for dark matter and other rare interactions*, *Nucl. Phys. B* **1003** (2024) 116473, [[arXiv:2404.19524](#)].
- [13] **SuperCDMS** Collaboration, R. Agnese et al., *Search for Low-Mass Weakly Interacting Massive Particles with SuperCDMS*, *Phys. Rev. Lett.* **112** (2014), no. 24 241302, [[arXiv:1402.7137](#)].
- [14] **SuperCDMS** Collaboration, K. Schneck et al., *Dark matter effective field theory scattering in direct detection experiments*, *Phys. Rev. D* **91** (2015), no. 9 092004, [[arXiv:1503.03379](#)].

- [15] **SuperCDMS** Collaboration, R. Agnese et al., *Projected Sensitivity of the SuperCDMS SNOLAB experiment*, *Phys. Rev. D* **95** (2017), no. 8 082002, [[arXiv:1610.00006](#)].
- [16] **SuperCDMS** Collaboration, R. Agnese et al., *Low-mass dark matter search with CDMSSlite*, *Phys. Rev. D* **97** (2018), no. 2 022002, [[arXiv:1707.01632](#)].
- [17] **NEWS-G** Collaboration, Q. Arnaud et al., *First results from the NEWS-G direct dark matter search experiment at the LSM*, *Astropart. Phys.* **97** (2018) 54–62, [[arXiv:1706.04934](#)].
- [18] **NEWS-G** Collaboration, M. M. A. et al., *Search for light dark matter with news-g at the lsm using a methane target*, [arXiv:2407.12769](#).
- [19] **NEWS-G** Collaboration, D. Durnford and M.-C. Piro, *The search for Light Dark Matter with NEWS-G*, *J. Phys. Conf. Ser.* **2156** (2021), no. 1 012059, [[arXiv:2111.02796](#)].
- [20] **NEWS-G** Collaboration, L. Balogh et al., *Exploring light dark matter with the DarkSPHERE spherical proportional counter electroformed underground at the Boulby Underground Laboratory*, *Phys. Rev. D* **108** (2023), no. 11 112006, [[arXiv:2301.05183](#)].
- [21] A. K. Drukier, K. Freese, and D. N. Spergel, *Detecting cold dark-matter candidates*, *Phys. Rev. D* **33** (Jun, 1986) 3495–3508.
- [22] N. Bozorgnia, F. Calore, M. Schaller, M. Lovell, G. Bertone, C. S. Frenk, R. A. Crain, J. F. Navarro, J. Schaye, and T. Theuns, *Simulated Milky Way analogues: implications for dark matter direct searches*, *JCAP* **1605** (2016), no. 05 024, [[arXiv:1601.04707](#)].
- [23] C. Kelso, C. Savage, M. Valluri, K. Freese, G. S. Stinson, and J. Bailin, *The impact of baryons on the direct detection of dark matter*, *JCAP* **1608** (2016) 071, [[arXiv:1601.04725](#)].
- [24] J. D. Sloane, M. R. Buckley, A. M. Brooks, and F. Governato, *Assessing Astrophysical Uncertainties in Direct Detection with Galaxy Simulations*, *Astrophys. J.* **831** (2016) 93, [[arXiv:1601.05402](#)].
- [25] N. Bozorgnia and G. Bertone, *Implications of hydrodynamical simulations for the interpretation of direct dark matter searches*, *Int. J. Mod. Phys.* **A32** (2017), no. 21 1730016, [[arXiv:1705.05853](#)].
- [26] N. Bozorgnia, A. Fattahi, C. S. Frenk, A. Cheek, D. G. Cerdeno, F. A. Gómez, R. J. Grand, and F. Marinacci, *The dark matter component of the Gaia radially anisotropic substructure*, *JCAP* **07** (2020) 036, [[arXiv:1910.07536](#)].
- [27] R. Poole-McKenzie, A. S. Font, B. Boxer, I. G. McCarthy, S. Burdin, S. G. Stafford, and S. T. Brown, *Informing dark matter direct detection limits with the ARTEMIS simulations*, *JCAP* **11** (2020) 016, [[arXiv:2006.15159](#)].
- [28] G. E. Lawrence, A. R. Duffy, C. A. Blake, and P. F. Hopkins, *Gusts in the Headwind: Uncertainties in Direct Dark Matter Detection*, [arXiv:2207.07644](#).
- [29] M. Kuhlen, A. Pillepich, J. Guedes, and P. Madau, *The Distribution of Dark Matter in the Milky Way’s Disk*, *Astrophys. J.* **784** (2014) 161, [[arXiv:1308.1703](#)].
- [30] T. Lacroix, A. Núñez Castiñeyra, M. Stref, J. Lavalley, and E. Nezri, *Predicting the dark matter velocity distribution in galactic structures: tests against hydrodynamic cosmological simulations*, *JCAP* **10** (2020) 031, [[arXiv:2005.03955](#)].
- [31] A. Smith-Orlik et al., *The impact of the Large Magellanic Cloud on dark matter direct detection signals*, *JCAP* **10** (2023) 070, [[arXiv:2302.04281](#)].
- [32] G. Besla, A. Peter, and N. Garavito-Camargo, *The highest-speed local dark matter particles come from the Large Magellanic Cloud*, *JCAP* **1911** (2019), no. 11 013, [[arXiv:1909.04140](#)].
- [33] K. Donaldson, M. S. Petersen, and J. Peñarrubia, *Effects on the local dark matter distribution due to the Large Magellanic Cloud*, *Mon. Not. Roy. Astron. Soc.* **L513** (2022), no. 1 46, [[arXiv:2111.15440](#)].

- [34] J. Fan, M. Reece, and L.-T. Wang, *Non-relativistic effective theory of dark matter direct detection*, *JCAP* **11** (2010) 042, [[arXiv:1008.1591](#)].
- [35] A. L. Fitzpatrick, W. Haxton, E. Katz, N. Lubbers, and Y. Xu, *The Effective Field Theory of Dark Matter Direct Detection*, *JCAP* **02** (2013) 004, [[arXiv:1203.3542](#)].
- [36] A. L. Fitzpatrick, W. Haxton, E. Katz, N. Lubbers, and Y. Xu, *Model Independent Direct Detection Analyses*, [arXiv:1211.2818](#).
- [37] N. Anand, A. L. Fitzpatrick, and W. C. Haxton, *Weakly interacting massive particle-nucleus elastic scattering response*, *Phys. Rev. C* **89** (2014), no. 6 065501, [[arXiv:1308.6288](#)].
- [38] J. B. Dent, L. M. Krauss, J. L. Newstead, and S. Sabharwal, *General analysis of direct dark matter detection: From microphysics to observational signatures*, *Phys. Rev. D* **92** (2015), no. 6 063515, [[arXiv:1505.03117](#)].
- [39] D. Tucker-Smith and N. Weiner, *Inelastic dark matter*, *Phys. Rev. D* **64** (2001) 043502, [[hep-ph/0101138](#)].
- [40] R. J. J. Grand, F. A. Gómez, F. Marinacci, R. Pakmor, V. Springel, D. J. R. Campbell, C. S. Frenk, A. Jenkins, and S. D. M. White, *The Auriga Project: the properties and formation mechanisms of disc galaxies across cosmic time*, *Mon. Not. Roy. Astron. Soc.* **467** (2017), no. 1 179–207, [[arXiv:1610.01159](#)].
- [41] R. J. J. Grand, F. Fragkoudi, F. A. Gómez, A. Jenkins, F. Marinacci, R. Pakmor, and V. Springel, *Overview and public data release of the Auriga Project: cosmological simulations of dwarf and Milky Way-mass galaxies*, *arXiv e-prints* (Jan., 2024) arXiv:2401.08750, [[arXiv:2401.08750](#)].
- [42] J. Schaye et al., *The EAGLE project: Simulating the evolution and assembly of galaxies and their environments*, *Mon. Not. Roy. Astron. Soc.* **446** (2015) 521–554, [[arXiv:1407.7040](#)].
- [43] R. A. Crain et al., *The EAGLE simulations of galaxy formation: calibration of subgrid physics and model variations*, *Mon. Not. Roy. Astron. Soc.* **450** (2015), no. 2 1937–1961, [[arXiv:1501.01311](#)].
- [44] V. Springel, *E pur si muove: Galilean-invariant cosmological hydrodynamical simulations on a moving mesh*, *Mon. Not. Roy. Astron. Soc.* **401** (2010) 791, [[arXiv:0901.4107](#)].
- [45] **Planck** Collaboration, P. A. R. Ade et al., *Planck 2015 results. XIII. Cosmological parameters*, *Astron. Astrophys.* **594** (2016) A13, [[arXiv:1502.01589](#)].
- [46] C. Power, J. F. Navarro, A. Jenkins, C. S. Frenk, S. D. M. White, V. Springel, J. Stadel, and T. R. Quinn, *The Inner structure of Lambda CDM halos. 1. A Numerical convergence study*, *Mon. Not. Roy. Astron. Soc.* **338** (2003) 14–34, [[astro-ph/0201544](#)].
- [47] A. Jenkins, *A new way of setting the phases for cosmological multiscale Gaussian initial conditions*, *MNRAS* **434** (Sept., 2013) 2094–2120, [[arXiv:1306.5968](#)].
- [48] P. Salucci, F. Nesti, G. Gentile, and C. F. Martins, *The dark matter density at the Sun’s location*, *Astron. Astrophys.* **523** (2010) A83, [[arXiv:1003.3101](#)].
- [49] M. C. Smith, S. H. Whiteoak, and N. W. Evans, *Slicing and dicing the Milky Way disk in SDSS*, *Astrophys. J.* **746** (2012) 181, [[arXiv:1111.6920](#)].
- [50] J. Bovy and S. Tremaine, *On the local dark matter density*, *Astrophys. J.* **756** (2012) 89, [[arXiv:1205.4033](#)].
- [51] S. Garbari, C. Liu, J. I. Read, and G. Lake, *A new determination of the local dark matter density from the kinematics of K dwarfs*, *Mon. Not. Roy. Astron. Soc.* **425** (2012) 1445, [[arXiv:1206.0015](#)].

- [52] L. Zhang, H.-W. Rix, G. van de Ven, J. Bovy, C. Liu, and G. Zhao, *The Gravitational Potential Near the Sun From SEGUE K-dwarf Kinematics*, *Astrophys. J.* **772** (2013) 108, [[arXiv:1209.0256](#)].
- [53] J. Bovy and H.-W. Rix, *A Direct Dynamical Measurement of the Milky Way’s Disk Surface Density Profile, Disk Scale Length, and Dark Matter Profile at $4 \text{ kpc} \lesssim R \lesssim 9 \text{ kpc}$* , *Astrophys. J.* **779** (2013) 115, [[arXiv:1309.0809](#)].
- [54] L. Posti and A. Helmi, *Mass and shape of the Milky Way’s dark matter halo with globular clusters from Gaia and Hubble*, *A&A* **621** (Jan, 2019) A56, [[arXiv:1805.01408](#)].
- [55] J. Buch, S. C. J. Leung, and J. Fan, *Using Gaia DR2 to Constrain Local Dark Matter Density and Thin Dark Disk*, *JCAP* **1904** (2019) 026, [[arXiv:1808.05603](#)].
- [56] P. J. McMillan, *Mass models of the Milky Way*, *Mon. Not. Roy. Astron. Soc.* **414** (2011) 2446–2457, [[arXiv:1102.4340](#)].
- [57] R. Catena and P. Ullio, *A novel determination of the local dark matter density*, *JCAP* **1008** (2010) 004, [[arXiv:0907.0018](#)].
- [58] M. Weber and W. de Boer, *Determination of the Local Dark Matter Density in our Galaxy*, *Astron. Astrophys.* **509** (2010) A25, [[arXiv:0910.4272](#)].
- [59] F. Iocco, M. Pato, G. Bertone, and P. Jetzer, *Dark Matter distribution in the Milky Way: microlensing and dynamical constraints*, *JCAP* **1111** (2011) 029, [[arXiv:1107.5810](#)].
- [60] F. Nesti and P. Salucci, *The Dark Matter halo of the Milky Way, AD 2013*, *JCAP* **1307** (2013) 016, [[arXiv:1304.5127](#)].
- [61] Y. Sofue, *Dark halos of M 31 and the Milky Way*, *Publ. Astron. Soc. Jap.* **67** (2015), no. 4 75, [[arXiv:1504.05368](#)].
- [62] M. Pato, F. Iocco, and G. Bertone, *Dynamical constraints on the dark matter distribution in the Milky Way*, *JCAP* **1512** (2015), no. 12 001, [[arXiv:1504.06324](#)].
- [63] P. F. de Salas, K. Malhan, K. Freese, K. Hattori, and M. Valluri, *On the estimation of the Local Dark Matter Density using the rotation curve of the Milky Way*, *JCAP* **10** (2019) 037, [[arXiv:1906.06133](#)].
- [64] F. Kahlhoefer, S. Kulkarni, and S. Wild, *Exploring light mediators with low-threshold direct detection experiments*, *JCAP* **11** (2017) 016, [[arXiv:1707.08571](#)].
- [65] M. Cirelli, E. Del Nobile, and P. Panci, *Tools for model-independent bounds in direct dark matter searches*, *JCAP* **10** (2013) 019, [[arXiv:1307.5955](#)].
- [66] R. Schönrich, J. Binney, and W. Dehnen, *Local kinematics and the local standard of rest*, *MNRAS* **403** (Apr., 2010) 1829–1833, [[arXiv:0912.3693](#)].
- [67] R. Catena and B. Schwabe, *Form factors for dark matter capture by the Sun in effective theories*, *JCAP* **04** (2015) 042, [[arXiv:1501.03729](#)].
- [68] R. Catena, *Dark matter directional detection in non-relativistic effective theories*, *JCAP* **07** (2015) 026, [[arXiv:1505.06441](#)].
- [69] **DarkSide-50** Collaboration, P. Agnes et al., *Effective field theory interactions for liquid argon target in DarkSide-50 experiment*, *Phys. Rev. D* **101** (2020), no. 6 062002, [[arXiv:2002.07794](#)].
- [70] **LUX** Collaboration, D. S. Akerib et al., *Constraints on effective field theory couplings using 311.2 days of LUX data*, *Phys. Rev. D* **104** (2021), no. 6 062005, [[arXiv:2102.06998](#)].
- [71] **SuperCDMS** Collaboration, M. F. Albakry et al., *Effective Field Theory Analysis of CDMSlite Run 2 Data*, [[arXiv:2205.11683](#)].
- [72] **DEAP** Collaboration, P. Adhikari et al., *Constraints on dark matter-nucleon effective couplings in the presence of kinematically distinct halo substructures using the DEAP-3600*

- detector, *Phys. Rev. D* **102** (2020), no. 8 082001, [[arXiv:2005.14667](#)]. [Erratum: *Phys.Rev.D* 105, 029901 (2022)].
- [73] **LZ** Collaboration, J. Aalbers et al., *First constraints on WIMP-nucleon effective field theory couplings in an extended energy region from LUX-ZEPLIN*, *Phys. Rev. D* **109** (2024), no. 9 092003, [[arXiv:2312.02030](#)].
- [74] **DARWIN** Collaboration, J. Aalbers et al., *DARWIN: towards the ultimate dark matter detector*, *JCAP* **11** (2016) 017, [[arXiv:1606.07001](#)].
- [75] **NEWS-G** Collaboration, L. Balogh et al., *The NEWS-G detector at SNOLAB*, *JINST* **18** (2023), no. 02 T02005, [[arXiv:2205.15433](#)].
- [76] **GAMBIT Dark Matter Workgroup** Collaboration, T. Bringmann et al., *DarkBit: A GAMBIT module for computing dark matter observables and likelihoods*, *Eur. Phys. J. C* **77** (2017), no. 12 831, [[arXiv:1705.07920](#)].
- [77] M. J. Bressler, *Operation and Calibration of Right-Side-Up Bubble Chambers at $\sim keV$ Thresholds: Towards New Superheated Dark Matter Searches*. PhD thesis, Drexel University, 2022.
- [78] X. Li and M.-C. Piro, *Model for bubble nucleation efficiency of low-energy nuclear recoils in bubble chambers for dark matter detection*, *Phys. Rev. D* **110** (2024), no. 2 022005, [[arXiv:2401.15531](#)].
- [79] **SuperCDMS** Collaboration, R. Agnese et al., *New Results from the Search for Low-Mass Weakly Interacting Massive Particles with the CDMS Low Ionization Threshold Experiment*, *Phys. Rev. Lett.* **116** (2016), no. 7 071301, [[arXiv:1509.02448](#)].